as a function of a control parameter. By extrapolation to $T = 0$ of both the Hall crossover and the magnetic phase transition[12], we infer that a large jump of the Hall coefficient occurs at the QCP. We expect this new insight, made possible primarily by the absence of superconductivity, to have broad implications for other strongly correlated electron systems[27]. □

Methods

Anomalous Hall effect

In general, the Hall effect of materials containing localized magnetic moments is dominated at high temperatures by an anomalous Hall effect produced by the left-right asymmetry in incoherent electron scattering processes[28]. The initial or linear-response Hall coefficient R_H (Hall coefficient in zero-field limit) scales for many materials with the product of electrical resistivity ρ and magnetic susceptibility χ,

$$R_H = R_0 + C\rho\chi \quad (3)$$

where R_0 is the normal Hall coefficient and C is a constant[28]. The term $C\rho\chi$ represents the anomalous Hall effect due to intrinsic scattering. The temperature-independent extrinsic anomalous Hall coefficient R_{ex} due to skew scattering by residual defects may be estimated from

$$R_{ex} = C\rho_0\chi_0 \quad (4)$$

where ρ_0 is the residual resistivity and χ_0 the residual volume magnetic susceptibility[28]. A model including crystalline electric field effects valid in the incoherent regime[29], on the other hand, predicts

$$R_H = R_0 + R_s\chi \quad (5)$$

instead of equation (3). Here R_s is a constant and $R_s\chi$ the anomalous Hall-effect term.

In Fig. 1a we have shown that also in $YbRh_2Si_2$ the high-temperature Hall coefficient is dominated by the anomalous Hall effect. Between 7 and 300 K (90 and 300 K), equation (3) (equation (5)) holds (compare inset of Fig. 1a). The R_0 value obtained for both models is $(2.4 \pm 0.1) \times 10^{-10}\,m^3\,C^{-1}$, which corresponds, in a simple one band model, to a charge carrier concentration of $2.6 \times 10^{28}\,m^{-3}$ (approximately 2 holes per formula unit of $YbRh_2Si_2$). Considering only the magnetic contribution to ρ in equation (3) yields similar values for R_0 (ref. 18). Below about 1 K, where the extrapolation of the fit according to equation (3) (red dashed curve in Fig. 1a) becomes temperature independent and saturates at the value of the normal Hall coefficient R_0, the intrinsic anomalous Hall effect is negligible. The extrinsic anomalous Hall effect estimated from equation (4) with $\rho_0 \approx 1\,\mu\Omega$ cm and $\chi_0 = 0.0035$ ($B \| c$, $T = 40$ mK) (ref. 12) is less than 4% of R_0 and thus plays a negligible role. Therefore, below about 1 K, the initial Hall coefficient of $YbRh_2Si_2$ is essentially free of any anomalous contribution.

The anomalous Hall effect in finite magnetic fields may, in analogy with equation (3), be estimated from

$$\rho_{H,a}(B) = C\rho(B)\mu_0 M(B) \quad (6)$$

where $\rho(B)$ and $M(B)$ are the field-dependent electrical resistivity and magnetization, respectively.

For $YbRh_2Si_2$, $\rho(B)$ (not shown) and $M(B)$ (ref. 12) have been measured in the relevant geometry ($B \| c$, current $I \perp c$). For the parameter C we use the value extracted from the temperature dependence of the initial Hall coefficient (inset of Fig. 1a). $\rho_{H,a}$ is less than 20% of ρ_H at all temperatures and fields.

Received 1 July; accepted 14 October 2004; doi:10.1038/nature03129.

1. Martin, R. M. Fermi-surface sum rule and its consequences for periodic Kondo and mixed-valence systems. *Phys. Rev. Lett.* **48,** 362–365 (1982).
2. Fulde, P. in *Narrow-Band Phenomena—Influence of Electrons with both Band and Localized Character* (ed. Fuggle, J. C.) 27–29 (Plenum, New York, 1988).
3. Oshikawa, M. Topological approach to Luttinger's theorem and Fermi surface of a Kondo lattice. *Phys. Rev. Lett.* **84,** 3370–3373 (2000).
4. Hertz, J. A. Quantum critical phenomena. *Phys. Rev. B* **14,** 1165–1184 (1976).
5. Millis, A. J. Effect of a nonzero temperature on quantum critical points in itinerant fermion systems. *Phys. Rev. B* **48,** 7183–7196 (1993).
6. Schröder, A. *et al.* Onset of antiferromagnetism in heavy-fermion metals. *Nature* **407,** 351–355 (2000).
7. Coleman, P., Pépin, C., Si, Q. & Ramazashvili, R. How do Fermi liquids get heavy and die? *J. Phys. Condens. Matter* **13,** R723–R738 (2001).
8. Si, Q., Rabello, S., Ingersent, K. & Smith, J. L. Locally critical quantum phase transitions in strongly correlated metals. *Nature* **413,** 804–808 (2001).
9. Trovarelli, O. *et al.* $YbRh_2Si_2$: Pronounced non-Fermi-liquid effects above a low-lying magnetic phase transition. *Phys. Rev. Lett* **85,** 626–629 (2000).
10. Ishida, K. *et al.* $YbRh_2Si_2$: Spin fluctuations in the vicinity of a quantum critical point at low magnetic fields. *Phys. Rev. Lett.* **89,** 107202 (2002).
11. Ishida, K. *et al.* Low-temperature magnetic order and spin dynamics in $YbRh_2Si_2$. *Phys. Rev. B* **68,** 184401 (2003).
12. Gegenwart, P. *et al.* Magnetic-field induced quantum critical point in $YbRh_2Si_2$. *Phys. Rev. Lett.* **89,** 056402 (2002).
13. Küchler, R. *et al.* Low-temperature thermal expansion and magnetostriction of $YbRh_2(Si_{1-x}Ge_x)_2$ ($x = 0$ and 0.05). *J. Magn. Magn. Mater.* **272–276,** 229–230 (2004).
14. Custers, J. *et al.* The break-up of heavy electrons at a quantum critical point. *Nature* **424,** 524–527 (2003).
15. Stewart, G. R. Non-Fermi-liquid behavior in *d*- and *f*-electron metals. *Rev. Mod. Phys.* **73,** 797–855 (2001).
16. Senthil, T., Vojta, M. & Sachdev, S. Weak magnetism and non-Fermi liquids near heavy-fermion critical points. *Phys. Rev. B* **69,** 035111 (2004).
17. Paschen, S. *et al.* Hall effect of the NFL compound $YbRh_2Si_2$. *Acta Phys. Polon. B* **34,** 359–362 (2003).
18. Paschen, S. *et al.* Anomalous Hall effect in $YbRh_2Si_2$. *Physica B* (in the press).
19. Anderson, P. W. Hall effect in the two-dimensional Luttinger liquid. *Phys. Rev. Lett.* **67,** 2092–2094 (1991).
20. Nakajima, Y. *et al.* Normal-state Hall angle and magnetoresistance in quasi-2D heavy fermion $CeCoIn_5$ near a quantum critical point. *J. Phys. Soc. Jpn* **73,** 5–8 (2004).
21. Custers, J. *Quantum-Critical Behavior in the Heavy-Fermion Compounds $YbRh_2Si_2$ and $CeIn_{3-x}Sn_x$.* PhD thesis, TU Dresden (2004).
22. Lee, M., Husmann, A., Rosenbaum, T. F. & Aeppli, G. High resolution study of magnetic ordering at absolute zero. *Phys. Rev. Lett.* **92,** 187201 (2004).
23. Haldane, F. D. M. 'Luttinger liquid theory' of one-dimensional quantum fluids: I. Properties of the Luttinger model and their extension to the general 1D interacting spinless Fermi gas. *J. Phys. C* **14,** 2585–2609 (1981).
24. Varma, C. M., Littlewood, P. B., Schmitt-Rink, S., Abrahams, E. & Ruckenstein, A. E. Phenomenology of the normal state of Cu-O high-temperature superconductors. *Phys. Rev. Lett.* **63,** 1996–1999 (1989).
25. Valla, T. *et al.* Evidence for quantum critical behaviour in the optimally doped cuprate $Bi_2Sr_2CaCu_2O_{8+\delta}$. *Science* **285,** 2110–2113 (1999).
26. Yeh, A. *et al.* Quantum phase transition in a common metal. *Nature* **419,** 459–462 (2002).
27. Balakirev, F. F. *et al.* Signature of optimal doping in Hall-effect measurements on a high-temperature superconductor. *Nature* **424,** 912–915 (2003).
28. Fert, A. & Levy, P. M. Theory of the Hall effect in heavy-fermion compounds. *Phys. Rev. B* **36,** 1907–1916 (1987).
29. Kontani, H., Miyazawa, M. & Yamada, K. Theory of anomalous Hall effect in a heavy fermion system with a strong anisotropic crystal field. *J. Phys. Soc. Jpn* **66,** 2252–2255 (1997).
30. Norman, M. R., Si, Q., Bazaliy, Y. B. & Ramazashvili, R. Hall effect in nested antiferromagnets near the quantum critical point. *Phys. Rev. Lett.* **90,** 116601 (2003).

Supplementary Information accompanies the paper on **www.nature.com/nature**.

Acknowledgements We acknowledge discussions with P. Bühler, J. Custers, C. Langhammer, C. Pépin, A. Rosch, A. Schofield, M. Vojta, A. Tsvelik and F. Weickert. Part of the work at Dresden was supported by the Fonds der Chemischen Industrie. P.C. and Q.S. are supported by the National Science Foundation. The work at Rice University was partially supported by the Welch Foundation and TCSAM.

Competing interests statement The authors declare that they have no competing financial interests.

Correspondence and requests for materials should be addressed to S.P. (paschen@cpfs.mpg.de).

Lensless imaging of magnetic nanostructures by X-ray spectro-holography

S. Eisebitt[1], J. Lüning[2], W. F. Schlotter[2,3], M. Lörgen[1], O. Hellwig[1,4], W. Eberhardt[1] & J. Stöhr[2]

[1]*BESSY mbH, Albert-Einstein-Straße 15, 12489 Berlin, Germany*
[2]*SSRL, Stanford Linear Accelerator Center, 2575 Sand Hill Road, Menlo Park, California 94025, USA*
[3]*Department of Applied Physics, 316 Via Pueblo Mall, Stanford University, Stanford, California 94305-4090, USA*
[4]*San Jose Research Center, Hitachi Global Storage Technologies, 650 Harry Road, San Jose, California 95120, USA*

Our knowledge of the structure of matter is largely based on X-ray diffraction studies of periodic structures and the successful transformation (inversion) of the diffraction patterns into real-space atomic maps. But the determination of non-periodic nanoscale structures by X-rays is much more difficult. Inversion of the measured diffuse X-ray intensity patterns suffers from the intrinsic loss of phase information[1,2], and direct imaging methods are limited in resolution by the available X-ray optics[3]. Here we demonstrate a versatile technique for imaging nanostructures, based on the use of resonantly tuned soft X-rays for scattering contrast and the direct Fourier inversion of a holo-

graphically formed interference pattern. Our implementation places the sample behind a lithographically manufactured mask with a micrometre-sized sample aperture and a nanometre-sized hole that defines a reference beam. As an example, we have used the resonant X-ray magnetic circular dichroism effect to image the random magnetic domain structure in a Co/Pt multilayer film with a spatial resolution of 50 nm. Our technique, which is a form of Fourier transform holography, is transferable to a wide variety of specimens, appears scalable to diffraction-limited resolution, and is well suited for ultrafast single-shot imaging with coherent X-ray free-electron laser sources[4].

Our indirect imaging technique is based on the use of tunable soft X-rays and simple Fourier inversion of a reciprocal space interference pattern to yield a real-space image. By tuning the energy of the X-rays to characteristic absorption edges we can generate contrast for different properties of the nanostructured sample, such as elemental and chemical composition. With further use of variable X-ray polarization the sensitivity and contrast is extended to charge[5] and spin orientations[6,7]. Our holography-based method overcomes the central problem of all indirect methods—the recovery of the phase information[2,8,9]—with the use of a nanoscale reference aperture next to the sample that phases the recorded interference pattern[1,10]. Our method is simple and suitable for imaging a variety of nanostructures, and the achievable resolution is, in principle, limited only by the soft X-ray wavelength, which is about a factor of ten smaller than the resolution achievable with image-forming X-ray lenses today.

This lensless spectro-holography technique does not require any kind of image-forming lenses, such as zone plates used in conventional X-ray microscopy[11] or electron optical lenses used for image formation in X-ray-induced photoemission electron microscopy[12]. Because holography-based methods require a coherence length that is longer than the optical path length differences encountered in the experiment, they have largely been restricted to lasers. For nanoscale applications, however, shorter-wavelength radiation is needed to overcome the diffraction-limited spatial resolution of conventional lasers[13]. In principle, X-rays allow higher spatial resolution, but in practice, submicrometre resolution has rarely been achieved[14], with the notable exceptions of refs 15 and 16, in which spatial resolutions of about 50 nm were achieved using combined holography and microscopy approaches[15,16].

Our studies use the high coherent flux and the polarization and photon-energy tunability available at advanced synchrotron radiation sources, such as the BESSY-II storage ring, where we carried out the present work. In particular, we use the large X-ray magnetic circular dichroism effect at the L-edges of the transition metals for image contrast[17] so that our method is a true combination of spectroscopy and holography. The new technique is complementary to direct magnetic X-ray imaging methods based on photoemission electron microscopy or transmission X-ray microscopy.

Our experimental arrangement is illustrated in Fig. 1. We used circularly polarized soft X-rays from an undulator source in conjunction with a spherical grating monochromator that determined the longitudinal coherence length. At the photon energy 778 eV (wavelength 1.59 nm) used in our study, corresponding to the Co L_3 absorption edge, the longitudinal coherence length was $\xi_l = \lambda^2/(2\Delta\lambda) = 1.6\,\mu$m, where λ is the wavelength. The beam from the monochromator was incident on an aperture of diameter $D = 20\,\mu$m that acted as a transverse coherence filter. The central Airy disk of the transmitted beam coherently illuminated a nanostructured transmission mask directly in front of the sample, both of which are placed $z = 723$ mm behind the coherence filter. This geometry determined the transverse coherence length of $\xi_t = (\lambda z)/(2\pi D) = 9.1\,\mu$m. An in-vacuum charge-coupled device (CCD) camera, positioned 315 mm downstream of the mask–sample structure, was used to record the hologram.

The key element in this experiment is the mask–sample arrangement. We chose an integrated mask–sample design, as illustrated in the lower inset of Fig. 1. The sample–mask structure was fabricated by use of a Si_3N_4 membrane on a Si support frame. On one side of the membrane we sputtered a 600-nm-thick gold film. Unlike the Si_3N_4 membrane, the thicker gold film is opaque for 778-eV X-rays. On the other side of the membrane a magnetic multilayer with 50 repeats of Co(4 Å)/Pt(7 Å) bilayers was sputter-deposited on a 20-nm-thick Pt base layer[18]. The multilayer was capped with a 2-nm Pt layer to prevent corrosion. We then used a focused ion beam to cut a circular aperture of diameter 1.5 μm out of the gold film, down to the Si_3N_4 membrane.

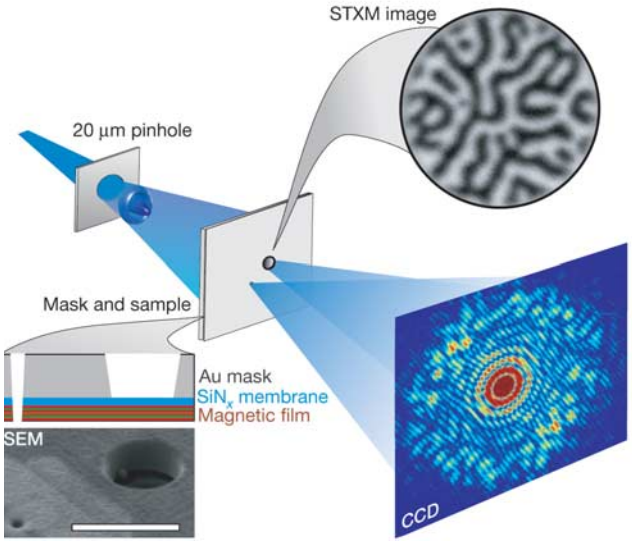

Figure 1 Scheme of the experimental set-up. Monochromatized and circular polarized X-rays are incident on a mask–sample structure after spatial coherence filtering. The object and reference beam are defined by the mask, and the resulting hologram is recorded on a CCD detector. The lower inset shows the geometry and an electron microscopy image of the mask–sample structure. The scale bar in the microscopy image is 2.0 μm. The top inset shows a STXM image of the magnetic structure illuminated through the sample aperture. The field of view is 1.5 μm.

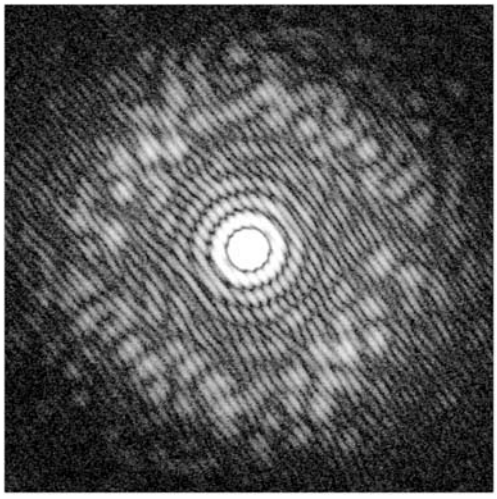

Figure 2 Hologram recorded with X-rays (right circular polarization) at a wavelength of 1.59 nm. The maximum in-plane momentum transfer in the measurement is $\pm 0.13\,\text{nm}^{-1}$, shown up to $\pm 0.06\,\text{nm}^{-1}$ in the image. Intensity is represented on a logarithmic grey scale, with black denoting the minimum intensity of 10^3 and white denoting the maximum intensity of 10^5. Black and white appear saturated in the picture only, the dynamic range of the hologram is 10^7.

This 'sample aperture' defines the object beam through the sample. An image of the magnetic domain structure within the sample aperture was recorded by scanning transmission X-ray microscopy[19] (STXM) and is shown in the upper inset of Fig. 1. It reveals a characteristic worm domain pattern where the black and white areas correspond to domains that have opposite out-of-plane magnetization directions[18]. Next to the sample aperture, at a centre-to-centre distance of 3 μm, a circular pinhole was drilled by a focused ion beam through the entire mask–sample structure. This high-aspect-ratio pinhole defines the reference beam. It had a conical shape along the beam direction with a diameter of 350 nm at the (Au) front side and 100 nm at the (multilayer) back side.

The in-plane reference hole and sample aperture conveniently define a lensless Fourier transform holography geometry[20,21]. The Fourier transform hologram recorded with circularly polarized soft X-rays of positive helicity is shown in Fig. 2. The incident intensity was adjusted so that the intense central peak in the hologram could be detected without saturation down to a minimum momentum transfer of $2\pi/(10\,\mu m)$. This led to typical exposure times of 10 s per frame. Fifty frames were accumulated to improve the counting statistics in the image. The Fraunhofer ring pattern dominating the centre of the hologram originates from the sample aperture with diameter 1.5 μm. A high-frequency oscillation created by the interference of object and reference wave is visible with high contrast. Small angle scattering caused by the magnetic domain structure[17,22,23] in the Co/Pt multilayer film is visible as a broad ring with an average momentum transfer of $|q| = 0.036\,nm^{-1}$. This small angle scattering ring is broken up into individual speckle attributable to object–object and object–reference interference.

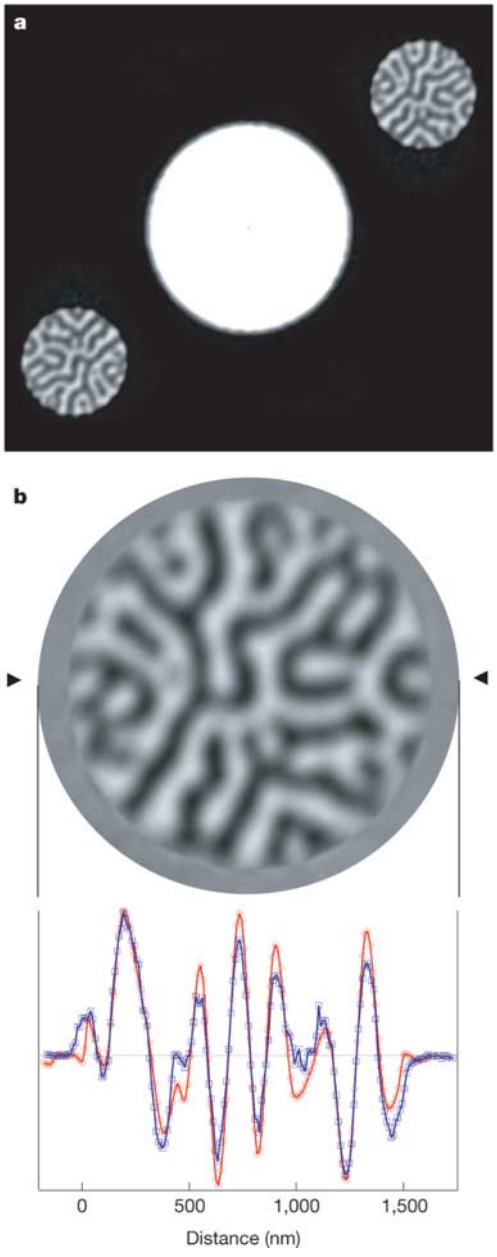

Figure 3 Images retrieved from the hologram. **a**, Two-dimensional fast Fourier transformation of the hologram in Fig. 2. **b**, Zoomed-in image, obtained by subtracting the Fourier transformations of opposite-helicity holograms. Below are shown scan lines through the holographic image (red) and the STXM image in Fig. 1 (blue).

Owing to the off-axis geometry in Fourier transform holography, the object image and its conjugate can easily be separated and retrieved by a single Fourier transformation of the scattering intensity[1]. In Fig. 3a we present a digital two-dimensional fast Fourier transformation of the magnetic X-ray hologram in Fig. 2. The intense area in the centre contains the sample–sample and reference hole–reference hole autocorrelations. The sample–reference hole cross-correlations are seen on opposite sides of the central structure. They contain the desired information and directly give a high-quality transmission image of the lateral magnetic domain structure. On helicity reversal of the incident soft X-rays, we observe in the image an inversion of the magnetic domain contrast as expected, while the mask contrast remains unaffected[23]. Therefore, as in magnetic spectro-microscopy, the difference of two opposite helicity images can be used to enhance the magnetic contrast and suppress any non-magnetic contributions. A helicity difference image is shown in Fig. 3b.

The magnetization map obtained by X-ray holography is in perfect agreement with the one obtained by STXM (Fig. 1, top right). Note that both have been recorded by exploiting the same dichroism contrast mechanism. This provides unambiguous proof that our lensless X-ray Fourier transform holography approach gives a unique real-space image of the sample.

To evaluate the spatial resolution, line scans through the magnetic profile obtained with spectro-microscopy and spectro-holography are compared in Fig. 3b. Both profiles are in quantitative agreement, indicating that the lateral resolution is essentially the same. The 10% to 90% contrast change in the image profiles has a width of 50 nm. The high spatial resolution is somewhat surprising, because in Fourier transform holography it is limited by the size of the reference source given in our case by the 100-nm diameter of the reference pinhole. Scanning electron microscopy (SEM) images show only the entrance and exit of the pinhole, so we cannot rule out the presence of a smaller constriction inside the high aspect ratio (1:8) pinhole channel. It is more likely, however, that the pinhole, tapered because of the 8° convergence of the focused ion beam, acts as a capillary waveguide and reduces the focal spot size[24].

Our experimental scheme, based on a nanostructured transmission mask on a transparent membrane, can be applied to a variety of different specimens. Samples can be grown directly on the back of a membrane, as presented here, or be introduced on a separate membrane and mounted in direct contact with the mask. Nanoparticles, colloids or biological samples could be placed into the object area in a controlled fashion by using, for example, integrated light microscopy and manipulator stages, as used for microinjection in biotechnology. Furthermore, one can easily envision an entire array of sample and reference apertures, allowing high-throughput investigations.

Our fixed arrangement of sample and reference aperture within the same plane greatly facilitates alignment, reduces the sensitivity to beam drift and eliminates focusing corrections in the holographic image reconstruction. It is also possible to record images with different well-defined shapes of the reference hole to apply appro-

priate source-shape corrections. The spatial resolution can be improved by using smaller apertures and through waveguide focusing effects, if it is not intensity-limited by the detectable maximum momentum transfer. When reducing the size of the reference aperture, either the X-ray transmission of the sample or the sample aperture size may have to be reduced to control the relative sample and reference beam intensities. If a reference beam intensity larger than the sample beam intensity cannot be achieved, nonlinearities in the holographic imaging process will have to be taken into account. A relative drift of the mask–sample structure relative to the CCD detector is not critical as long as it is smaller than the CCD pixel size (13.5 μm). Vibration isolation and thermal stabilization is therefore easy in comparison with other submicrometre microscopy techniques. Furthermore, extreme sample environments such as high magnetic fields or low temperatures can easily be implemented because there are no stringent space constraints around the sample.

Another exciting possibility is an improvement in spatial resolution by application of iterative phase retrieval methods[2,8,9,25] to the hologram. Our mask-based X-ray Fourier transform holography approach is fully compatible with iterative phase retrieval, provided that the hologram is recorded with sufficient resolution. In a combined approach we record a high-resolution X-ray hologram and the holographic image obtained by Fourier transformation is then used as the starting point for iterative refinement of the phase. In this way, ambiguities in the iterative process are restricted to the finest details of the image below the resolution of the holographic image. The ultimate resolution is then determined not by the reference pinhole size but by the maximum photon momentum transfer or, eventually, by the wavelength.

The present work was in part motivated by the expected availability of X-ray free-electron lasers in the near future[26,27]. Such sources will provide coherent high-intensity X-ray pulses of femtosecond duration. From the exposure time and coherent flux used for our images we can estimate that a single X-ray free-electron laser pulse will be sufficient to record an ultrafast single shot image. This will open the door for taking ultrafast movies of processes on the nanometre length scale, for example, of phase transitions. Our holographic approach is well matched to the spatial and temporal source properties of a free-electron laser and is the method of choice for single-shot ultrafast imaging with such sources[4]. □

Methods

Soft X-rays with circular polarization are generated in a APPLE-II-type helical undulator with 30 periods of length 56 mm. An energy resolution of $\lambda/\Delta\lambda = 2{,}000$ was obtained with a spherical grating monochromator. The 20-μm diameter aperture used for spatial filtering was located 6 m downstream of the beamline focus, thus accepting approximately 0.1% of the total beamline photon flux. Holograms were recorded with a Princeton Instruments PI-SX CCD camera equipped with an in-vacuum back-illuminated chip of 2,048 × 2,048 pixels of width 13.5 μm. For the hologram shown in Fig. 2, about 1×10^{10} photons were incident on the CCD chip during the accumulated exposure time. The apertures of the Fourier transform holography mask were prepared with a dual-beam focused ion beam instrument from FEI (Strata 235). The scanning X-ray microscopy image was recorded on the microscopy station on beamline 11 at the Advanced Light Source, Berkeley. The microscope has been described by ref. 19.

Received 8 July; accepted 28 October 2004; doi:10.1038/nature03139.

1. Stroke, G. W. *An Introduction to Coherent Optics and Holography* (Academic, New York, 1969).
2. Miao, J. W., Charalambous, P., Kirz, J. & Sayre, D. Extending the methodology of X-ray crystallography to allow imaging of micrometre-sized non-crystalline specimens. *Nature* **400,** 342–344 (1999).
3. Chao, W. L. *et al.* 20-nm-resolution soft x-ray microscopy demonstrated by use of multilayer test structures. *Opt. Lett.* **28,** 2019–2021 (2003).
4. Neutze, R., Wouts, R., Van der Spoel, D., Weckert, E. & Hajdu, J. Potential for biomolecular imaging with femtosecond X-ray pulses. *Nature* **406,** 752–757 (2000).
5. Ade, H. & Hsiao, B. X-ray linear dichroism microscopy. *Science* **262,** 1427–1429 (1993).
6. Stöhr, J. *et al.* Element-specific magnetic microscopy with circularly polarized X-rays. *Science* **259,** 658–661 (1993).
7. Fischer, P. *et al.* Magnetic domain imaging with a transmission X-ray microscope. *J. Magn. Magn. Mater.* **199,** 624–627 (1999).
8. Gerchberg, R. W. & Saxton, W. O. Practical algorithm for determination of phase from image and diffraction plane pictures. *Optik* **35,** 237–246 (1972).
9. Fienup, J. R. Phase retrieval algorithms—a comparison. *Appl. Opt.* **21,** 2758–2769 (1982).
10. Gabor, D., Kock, W. E. & Stroke, G. W. Holography. *Science* **173,** 11–23 (1971).
11. Focus on X-ray microscopy. *Synchrotron Radiat. News* (special issue, ed. Schmahl, G.) **16**(3), 2–63 (2003).
12. Stöhr, J. *et al.* Element-specific magnetic microscopy with circularly polarized X-rays. *Science* **259,** 658–661 (1993).
13. Xu, W. B., Jericho, M. H., Meinertzhagen, I. A. & Kreuzer, H. J. Digital in-line holography for biological applications. *Proc. Natl Acad. Sci. USA* **98,** 11301–11305 (2001).
14. Trebes, J. E. *et al.* Demonstration of X-ray holography with an X-ray laser. *Science* **238,** 517–519 (1987).
15. McNulty, I. *et al.* High-resolution imaging by Fourier-transform X-ray holography. *Science* **256,** 1009–1012 (1992).
16. Lindaas, S., Howells, H., Jacobsen, C. & Kalinovsky, A. X-ray holographic microscopy by means of photoresist recording and atomic-force microscope readout. *J. Opt. Soc. Am. A Opt. Image Sci. Vis.* **13,** 1788–1800 (1996).
17. Hannon, J. P., Trammell, G. T., Blume, M. & Gibbs, D. X-ray resonance exchange scattering. *Phys. Rev. Lett.* **61,** 1245–1248 (1988).
18. Hellwig, O., Denbeaux, G. P., Kortright, J. B. & Fullerton, E. E. X-ray studies of aligned magnetic stripe domains in perpendicular multilayers. *Physica B Condens. Matter* **336,** 136–144 (2003).
19. Kilcoyne, A. L. D. *et al.* Interferometer-controlled scanning transmission X-ray microscopes at the Advanced Light Source. *J. Synchrotron Radiat.* **10,** 125–136 (2003).
20. Stroke, G. W. Lensless Fourier-transform method for optical holography. *Appl. Phys. Lett.* **6,** 201–203 (1965).
21. Winthrop, J. T. & Worthing, C. R. X-ray microscopy by successive Fourier transformation. *Phys. Lett.* **15,** 124–126 (1965).
22. Kortright, J. B. *et al.* Soft-x-ray small-angle scattering as a sensitive probe of magnetic and charge heterogeneity. *Phys. Rev. B* **64,** 92401 (2001).
23. Eisebitt, S. *et al.* Polarization effects in coherent scattering from magnetic specimen: Implications for x-ray holography, lensless imaging, and correlation spectroscopy. *Phys. Rev. B* **68,** 104419 (2003).
24. Bergemann, C., Keymeulen, H. & Van der Veen, J. F. Focusing X-ray beams to nanometer dimensions. *Phys. Rev. Lett.* **91,** 204801 (2003).
25. Fienup, J. R. Reconstruction of a complex-valued object from the modulus of its Fourier transform using a support constraint. *J. Opt. Soc. Am.* **4,** 118–123 (1987).
26. Cho, A. The ultimate bright idea. *Science* **296,** 1008–1010 (2002).
27. Emma, P. *et al.* Femtosecond and subfemtosecond X-ray pulses from a self-amplified spontaneous-emission–based free-electron laser. *Phys. Rev. Lett.* **92,** 074801 (2004).

Acknowledgements We thank Y. Acremann for recording the STXM image of the sample at the Advanced Light Source and E. E. Fullerton for access to his thin film deposition facility. The work of the SSRL authors is supported by the US Department of Energy, Office of Basic Energy Sciences.

Competing interests statement The authors declare that they have no competing financial interests.

Correspondence and requests for materials should be addressed to S.E. (eisebitt@bessy.de) or J.L. (luning@stanford.edu).

High temperatures in the Late Cretaceous Arctic Ocean

Hugh C. Jenkyns[1], Astrid Forster[2], Stefan Schouten[2] & Jaap S. Sinninghe Damsté[2]

[1]*Department of Earth Sciences, University of Oxford, Parks Road, Oxford OX1 3PR, UK*
[2]*Royal Netherlands Institute for Sea Research (NIOZ), Department of Marine Biogeochemistry and Toxicology, PO Box 59, 1790 AB Den Burg, Texel, The Netherlands*

To understand the climate dynamics of the warm, equable greenhouse world of the Late Cretaceous period, it is important to determine polar palaeotemperatures. The early palaeoceanographic history of the Arctic Ocean has, however, remained largely unknown, because the sea floor and underlying deposits are usually inaccessible beneath a cover of floating ice. A shallow piston core taken from a drifting ice island in 1970 fortuitously retrieved unconsolidated Upper Cretaceous organic-rich sediment from Alpha ridge[1–4], a submarine elevated feature of probable oceanic origin[5]. A lack of carbonate in the sediments from this core has prevented the use of traditional oxygen-isotope palaeothermometry. Here we determine Arctic palaeotemperatures from these Upper Cretaceous deposits using TEX_{86},